Dynamic Performance Improvement of a Grid-Tied PV System Using a Feed-Forward Control Loop Acting on the NPC Inverter Currents

Leonardo Bruno Garcia Campanhol, Sérgio Augusto Oliveira da Silva, *Member, IEEE*, Azauri Albano de Oliveira, Jr., and Vinícius Dário Bacon

***Abstract*—This paper presents a three-phase grid-connected photovoltaic (PV) system, which is implemented using the neutral-point-clamped (NPC) inverter. A current feed-forward control loop (FFCL) is proposed to improve the PV system dynamic behavior, due to the PV array being constantly subjected to sudden solar irradiance change, which causes voltage oscillations in the dc bus and, hence, interferes in proper PV system operation. As the current FFCL acts to speed up the calculation of the inverter current references, the dynamic response of the currents injected into the grid is improved. As a consequence, the dynamic behavior of the dc-bus voltage is also enhanced, reducing both settling time and overshoot. Besides the injection of active power into the grid, the PV system is also controlled to perform active power-line conditioning, so that load harmonic currents are suppressed, as well as load reactive power is compensated. However, the NPC inverter must be properly designed to guarantee that its power rating will not be exceeded, since both fundamental and nonfundamental current components flow through the grid-tied inverter. Extensive experimental results based on a digital signal processor are presented in order to evaluate the effectiveness, as well as the static and dynamic performance of the PV system.**

***Index Terms*—Active power-line conditioning, feed-forward control loop (FFCL), photovoltaic (PV) system, three-level neutral-point-clamped (NPC) inverter.**

I. Introduction

IN RECENT years, the generation of electric energy based on renewable energy sources (RES) has risen significantly, due to growing demand for electricity, as well as reaching goals related to a reduction in the environmental and economic impacts introduced by conventional power generation pollutant sources. Thereby, the traditional setting of power generation has changed, highlighting the use of RES, such as hydro, biomass, wind, solar, and others.

Concerning the use of solar energy, this has been employed through the conversion of photovoltaic (PV) energy into electrical energy. In addition, this form of energy production can be considered clean, producing reduced environmental impacts, since the waste is generated only in the manufacturing process or in the disposal. For this reason, the generation of electricity by means of PV systems is considered promising among the various existing RES.

Usually, one or two power conversion stages are required to compose a grid-connected PV system. In double-stage PV systems, one power stage is a dc/dc converter and the other is a dc/ac converter [1]–[4]. In this case, the dc/dc converter performs the maximum power point tracking (MPPT) control, while the dc/ac converter connects the PV system to the grid and performs the current control.

On the other hand, in single-stage grid-tied PV systems [5]–[12], the control loops of the MPPT and inverter currents are, simultaneously, carried out in one power conversion stage. As a result, the power loss decreases, and hence, the system efficiency increases [7]. Furthermore, the speed of the MPPT control loop (dc-bus control loop) must be much slower than that of the current control loop, in order to ensure undistorted currents injected into the grid [12].

Nonuniform insolation and/or temperature variation interfere in the amount of energy generated by the PV system. Thus, independent of the PV system arrangement, techniques for achieving MPPT have been developed [12]–[15], where the tracking factor [15], complexity, and dynamic response are some of the main factors used to evaluate and/or compare MPPT algorithms.

PV arrays are also subjected to sudden solar radiation changes. In this case, the dc-bus voltage amplitude varies, and oscillations in the dc-bus voltage can occur. As a consequence, the performance of the PV system can be affected, since the dc-bus power balance is used to control the amplitude of the inverter currents injected into the grid. In other words, large

Manuscript received April 27, 2016; revised June 30, 2016 and August 19, 2016; accepted October 7, 2016. Date of publication November 7, 2016; date of current version February 9, 2017. This work was supported in part by CNPq under Grant 471825/2009-3.

L. B. G. Campanhol is with the Department of Electrical Engineering, Federal University of Technology (UTFPR-AP), Apucarana 86812-460, Brazil (e-mail: campanhol@utfpr.edu.br).

S. A. O da Silva and V. D. Bacon are with the Department of Electrical Engineering, Federal University of Technology (UTFPR-CP), Cornélio Procópio 86300-000, Brazil (e-mail: augus@utfpr.edu.br; viniciusbacon@utfpr.edu.br).

A. A. de Oliveira, Jr., is with the Department of Electrical and Computing Engineering, São Carlos Engineering School, University of São Paulo, São Carlos 13566-590, Brazil (e-mail: azauri@sc.usp.br).

Color versions of one or more of the figures in this paper are available online at http://ieeexplore.ieee.org.

Digital Object Identifier 10.1109/TIE.2016.2625779

0278-0046 © 2016 IEEE. Personal use is permitted, but republication/redistribution requires IEEE permission.
See http://www.ieee.org/publications_standards/publications/rights/index.html for more information.

voltage variations in the dc-bus interfere in the calculation of the grid-tied inverter current references during transients.

Most of the MPPT techniques presented in the literature do not consider or discuss the effects of abrupt variations in solar irradiance on the PV system performance. In [5], a feed-forward current (FFC) control loop was proposed to make the PV system dynamics independent from those of the distribution network and the loads. However, the effects of abrupt solar radiation variations on the PV system performance have not been treated. In [7], MPPT techniques were implemented taking into account a single-stage PV system operating under partial shading. Although the performance of the MPPT techniques was evaluated, no procedure was adopted to mitigate problems related to fast irradiance variations. A function-based MPPT method was proposed in [13], in order to evaluate the performance of the method with regard to start-up, steady-state, and dynamic response, considering abrupt solar radiation changes. The mentioned function is used to determine the duty cycle of the dc/dc converter employed to achieve the MPPT. On the other hand, the dynamic behavior of the dc-bus voltage has not been evaluated due to the proposed MPPT algorithm not having been tested, either using simulations or experimentation, in practical grid-tied PV systems. In [12], a modified incremental conductance MPPT algorithm is proposed to improve the stability of the MPPT method, when a single-stage grid-tied PV system is subjected to sudden insolation changes. Although this modified MMPT method acts detecting the fast decreasing of the PV array output power when abrupt insolation occurs, large dc-bus voltage oscillation is still observed during the aforementioned transient. In addition, this MPPT method is not able to detect fast increasing of the PV array output power when sudden isolation occurs.

This paper proposes implementation of a current feed-forward control loop (FFCL), which acts to speed up the calculation of the inverter current references and, hence, contributes to overcome problems associated with sudden increase and decrease solar radiation changes in grid-connected PV systems. The FFCL, which is not tied to any MPPT technique, acts in conjunction with the inverter dc-bus voltage controller, improving the dynamic response of both dc-bus voltage and inverter currents. As a consequence, the settling time and overshoot/undershoot are reduced during transient conditions. In addition, since the inverter dc-bus voltage oscillations are attenuated, the risk of over voltage rating in the power semiconductors is also reduced.

In this paper, besides the injection of active power into the grid, the PV system performs the active power-line conditioning task, which includes load harmonic current suppression and load reactive power compensation [3], [6], [16]–[18]. In this case, the PV system handles, simultaneously, the active energy produced by the PV array and both nonfundamental and/or fundamental nonactive energy, which are caused by harmonic currents/voltages or reactive currents, respectively [19]. In other words, the PV system is also able to carry out the parallel active power filter function, such that an effective power factor (PF) correction is performed.

Thus, in order to mitigate power quality problems and increase the system efficiency, the three-phase transformerless grid-tied PV system presented in this paper uses a single-stage dc/ac power conversion, which is implemented using the three-level neutral-point-clamped (3L-NPC) inverter [16], [20].

A current reference generator (CRG) algorithm calculates the reference current that will be synthetized by the grid-tied inverter. Once the active power-line conditioning is also taken into account, the following tasks are allowed:

1) injection of active power into the grid from the energy produced by the PV array;
2) compensation of the load reactive power;
3) suppression of the load harmonic currents.

However, due to the active conditioning operation, control of the ac current amplitude must be performed to avoid the occurrence of over power rating in the grid-tied inverter [6], [7].

The algorithm used to generate the references of the nonactive currents (harmonic and reactive components) is implemented based on the synchronous reference frame (SRF) method. Furthermore, the synchronous unit vector coordinates, $\sin(\theta)$ and $\cos(\theta)$, are calculated using the estimated utility voltage phase angle (θ), which is obtained from a phase-locked loop (PLL) system.

This paper is organized as follows. In Section II, the PV system description is presented, including the SRF-based CRG algorithm and the inverter current and dc-bus voltage controllers. Section III presents the FFCL and three-phase power-based PLL system (3pPLL) description. Section IV presents the controller design of the 3L-NPC inverter, where the open-loop and closed-loop transfer functions (TFs) of the current and voltage control loops are achieved. In addition, the procedures used to compute the voltage and current controller gains are presented. In Section V, the performance and feasibility of the single-stage three-phase grid-tied PV system are evaluated by means of extended experimental results. Finally, Section VI presents the conclusions.

II. PV System Description

Fig. 1 presents the complete scheme of the three-phase transformerless grid-tied PV system studied in this paper. As can be seen, the PV system is connected to the three-phase four-wire system, where, besides the injection of active energy into the grid, the active power-line conditioning is also carried out. As can be observed in Fig. 1, the single-stage PV system is implemented using the grid-connected 3L-NPC inverter, which has been widely used in applications involving PV systems [2], [8], [10].

Since single-stage power conversion is used in the PV system, the PV array is directly linked to the inverter dc-bus. The series-connected PV array string is composed of 20 series-connected solar panels. Under standard test conditions, the voltage of each panel at maximum power point (MPP) is around 30.8 V, resulting in a total dc-bus voltage of around 616 V at the PV array output terminals. Thus, the direct connection between the PV array and the inverter dc-bus is possible, and the use of any dc/dc step-up converter is not required. Therefore, the energy efficiency involving the power conversion stages increases and the overall system cost decreases.

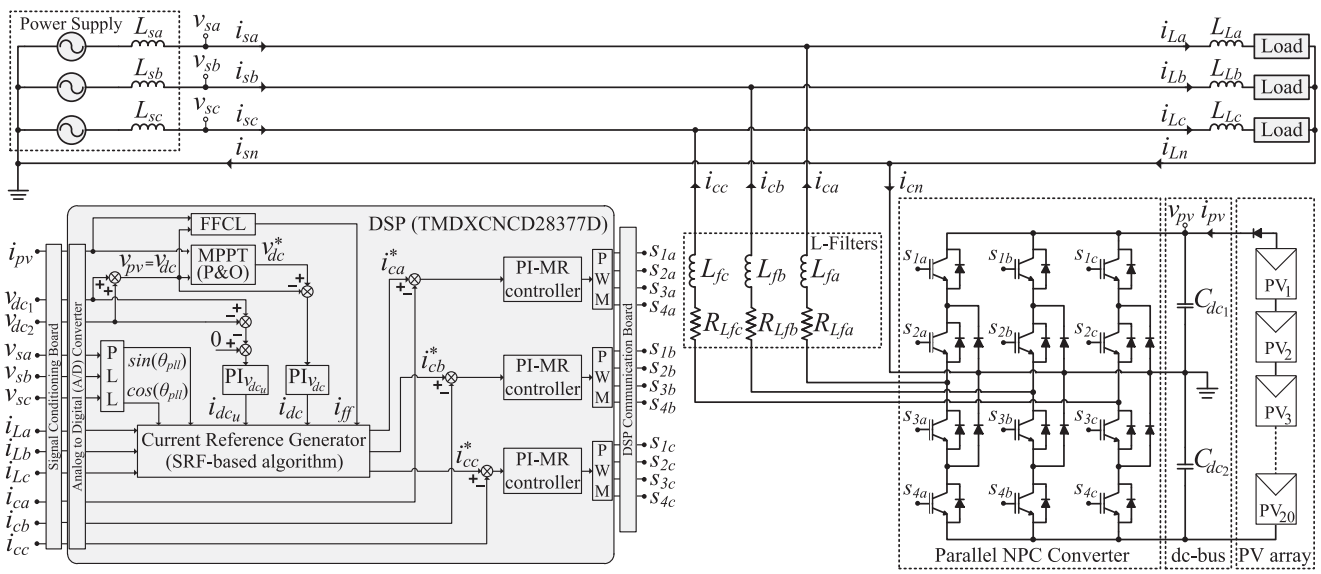

Fig. 1. Complete scheme of the single-stage three-phase grid-tied PV system.

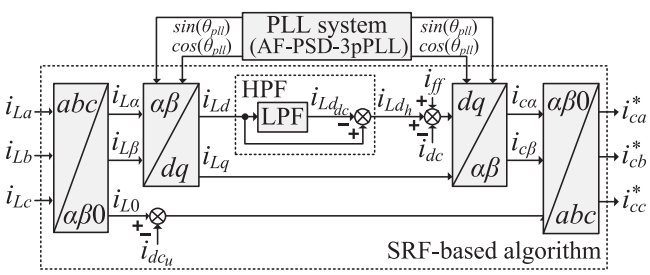

Fig. 2. Block diagram of the SRF-based CRG algorithm.

The NPC inverter is connected to the utility grid by means of inductive coupling filters (L-filters). As the NPC inverter is current controlled, its current references are computed in the control system shown in Fig. 1. All the algorithms employed to generate the inverter current references (SRF-based current and PLL), as well as the ac-current control loop and the other two dc-bus voltage control loops, will be properly described in the next subsections.

A. CRG Algorithm

In this subsection, the CRG, which is represented by the algorithm shown in Fig. 2, is described. It is employed to compute the proper grid-tied inverter current references (i^*_{ca}, i^*_{cb}, i^*_{cc}), which involve both the active and nonactive current components. In Fig. 2, the active current components are represented by $i_{\rm dc}$ and $i_{\rm ff}$, while i_{Ld_h}, i_{Lq} and i_{L0} represent the nonactive components.

The algorithm presented in Fig. 2 is based on the SRF method. In this SRF-based algorithm, the load currents are measured and transformed from a three-phase stationary frame (*abc*-axes) into a two-phase stationary frame ($\alpha\beta 0$ -axes). Next, these currents are transformed into a two-phase SRF (*dq*-axes). These transformations are given by (1) and (2), respectively,

$$\begin{bmatrix} i_{L\alpha} \\ i_{L\beta} \\ i_{L0} \end{bmatrix} = \sqrt{\frac{2}{3}} \begin{bmatrix} 1 & -\frac{1}{2} & -\frac{1}{2} \\ 0 & \frac{\sqrt{3}}{2} & -\frac{\sqrt{3}}{2} \\ \frac{1}{\sqrt{2}} & \frac{1}{\sqrt{2}} & \frac{1}{\sqrt{2}} \end{bmatrix} \begin{bmatrix} i_{La} \\ i_{Lb} \\ i_{Lc} \end{bmatrix} \tag{1}$$

$$\begin{bmatrix} i_{Ld} \\ i_{Lq} \end{bmatrix} = \begin{bmatrix} \cos\theta & \sin\theta \\ -\sin\theta & \cos\theta \end{bmatrix} \begin{bmatrix} i_{L\alpha} \\ i_{L\beta} \end{bmatrix}. \tag{2}$$

In the *dq*-axes, the current i_{Ld} is composed of both continuous and alternate components. The continuous component ($i_{Ld_{\rm dc}}$) represents the load fundamental active currents, while the alternate component (i_{Ld_h}) represents the load harmonic currents, both in the *d*-axis. The quantity i_{Ld_h} is extracted using a high-pass filter (HPF), where its implementation makes use of a low-pass filter (LPF), as shown in Fig. 2. In addition, the current i_{Ld} represents the sum of the load fundamental reactive component with the harmonic components in the *q*-axis, whereas i_{L0} represents the zero-sequence component of the neutral wire in the $\alpha\beta 0$ -axes. Therefore, in order to guarantee, in theory, unity PF, both i_{Lq}, i_{L0} and i_{Ld_h} quantities must be compensated.

As aforementioned, the inverter handles both active and nonactive currents. Thus, to guarantee that all active energy produced by the PV generator is injected into the grid without inverter over power rating, the amplitude of compensation currents, represented by i_{Ld_h}, must be controlled. For this purpose, the strategy employed in [6] was adopted in this paper.

The inverse transformations from the rotating reference frame *dq* into the $\alpha\beta$ reference frame and from the $\alpha\beta 0$ reference frame into the *abc* reference frame are given by (3) and (4), respectively. Hence, the final grid-tied inverter current references

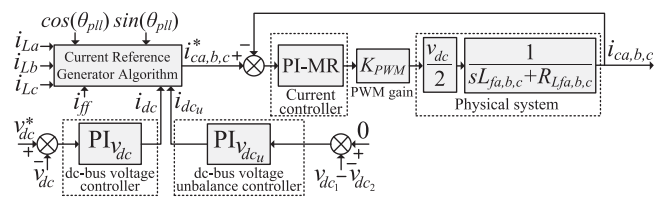

Fig. 3. Block diagram of the current and dc-bus control loops.

$(i^*_{ca}, i^*_{cb}, i^*_{cc})$ are obtained

$$\begin{bmatrix} i_{c\alpha} \\ i_{c\beta} \end{bmatrix} = \begin{bmatrix} \cos\theta & -\sin\theta \\ \sin\theta & \cos\theta \end{bmatrix} \begin{bmatrix} i_{Ldh} + i_{\mathrm{ff}} - i_{\mathrm{dc}} \\ i_{Lq} \end{bmatrix} \tag{3}$$

$$\begin{bmatrix} i^*_{ca} \\ i^*_{cb} \\ i^*_{cc} \end{bmatrix} = \sqrt{\frac{2}{3}} \begin{bmatrix} 1 & 0 & \frac{1}{\sqrt{2}} \\ -\frac{1}{2} & \frac{\sqrt{3}}{2} & \frac{1}{\sqrt{2}} \\ -\frac{1}{2} & -\frac{\sqrt{3}}{2} & \frac{1}{\sqrt{2}} \end{bmatrix} \begin{bmatrix} i_{c\alpha} \\ i_{c\beta} \\ i_{L0} - i_{\mathrm{dc}_u} \end{bmatrix}. \tag{4}$$

The currents i_{dc} and i_{dc_u} represented in (3) and (4), respectively, are extracted from their respective dc-bus voltage controllers, as shown in Fig. 3. In addition, the FFC i_{ff} represented in (3) is obtained from the FFCL. The difference between i_{ff} and i_{dc} $(i_{\mathrm{ff}} - i_{\mathrm{dc}})$ shown in Fig. 3 performs the dc-bus active power balance of the PV system, as well as controls the active power demanded to regulate the dc-bus voltage, considering the compensation of the power loss related to the L-filters and switching devices. Details related to the FFC control action are discussed in Section III.

B. Current Controller

The current controller (proportional-integral multiresonant—PI-MR) used in the *abc* phases of the PV system is shown in Fig. 3, where the physical system is represented by the inductances $(L_{fa,b,c})$ and resistances $(R_{Lfa,b,c})$ of the L-filters (see Fig. 1), in conjunction with the dc-bus voltage $(v_{\mathrm{dc}}/2)$. The NPC inverter pulse width modulation (PWM) static gain is represented by K_{PWM}, which is calculated taking into account the peak value of the PWM triangular carrier [22].

Since only alternate components compose the inverter current references $(i^*_{ca}, i^*_{cb}, i^*_{cc})$, the conventional proportional-integral (PI) controller does not guarantee null error in steady state. Thus, the PI-MR controller is adopted. The TF of the PI-MR controller is given by (5), in which, due to the infinite open-loop gain at the resonant frequency (ω_o), zero steady-state error is achieved

$$G_{\mathrm{PI-MR}}(s) = k_{Pi} + \frac{k_{Ii}}{s} + \sum_{m=1}^{n} \frac{k_m s}{(s^2 + (m\omega_1)^2)}$$
$$= G_{\mathrm{PI}}(s) + \sum_{m=1}^{n} G_{\mathrm{MR}(m)}(s). \tag{5}$$

In (5), k_{Pi} and k_{Ii} represent the respective proportional and integral gains of the current PI-MR controller; the resonant gain at a specific resonant frequency $(\omega_o = m\omega_1)$ is represented by k_m; ω_1 is the fundamental utility frequency; and as $m = 1$, 3, 5, 7, and 9, the first, third, fifth, seventh, and ninth components were chosen as resonant terms. The first-order component $(m = 1)$ represents both the fundamental active components injected into the utility grid and the fundamental load reactive components.

On the other hand, the multiresonant PI controllers (see Fig. 3) are tuned so that the resonant terms present 0 dB gain at their respective crossover frequencies (ω_{cm}). Thus, the multiresonant controller gains (k_m), presented in (5), are achieved to guarantee that the multiresonant crossover frequencies will be equal to the adopted crossover frequency defined in the design specifications of the current PI controllers (ω_{ci}), such that $\omega_{\mathrm{cm}} = \omega_{\mathrm{ci}}$.

C. DC-Bus Controllers

As can be seen, two dc-bus voltage PI controllers are also presented in Fig. 3. The first, denominated $\mathrm{PI}_{v_{\mathrm{dc}}}$, is used to control the total dc-bus voltage at a constant reference v^*_{dc}. The reference voltage v^*_{dc} is obtained from the perturb and observe (P&O)-based MPPT technique [6], as shown in Fig. 1. The output signal of this controller is represented by i_{dc}, where this quantity represents the total energy produced by the PV system plus the energy demanded by the PV system to compensate the losses related to the filtering inductors and semiconductor devices. The current i_{dc} is included in (3) and represented in Figs. 2 and 3. The second dc-bus controller, denominated $\mathrm{PI}_{v_{\mathrm{dc}_u}}$, is used to compensate the dc-bus voltage unbalances. In this case, the difference between the dc-bus voltages $(v_{\mathrm{dc}_1} - v_{\mathrm{dc}_2})$ is measured and compared to zero reference, as shown in Figs. 1 and 3. The $\mathrm{PI}_{v_{\mathrm{dc}_u}}$ output signal (i_{dc_u}) is included in (4) and also represented in Figs. 2 and 3.

III. Current FFCL

Atmospheric conditions related to solar radiance and/or temperature imply in distinct amounts of energy available in the PV array. In particular, abrupt solar radiation changes result in voltage oscillations in the inverter dc bus, affecting computation of the inverter current references, and interfering in the proper operation of the PV system.

The FFCL proposed in this paper aims to reduce the amplitude oscillations that can occur in the dc-bus voltage due to the occurrence of disturbances, such as sudden insolation changes. This control action is represented by the FFC (i_{ff}) shown in Fig. 2.

The FFCL is based on the dc-bus power balance. Although maintaining the dc-bus voltage by means of only the dc-bus voltage controller could ensure PV system power balance, this controller is not fast enough to avoid voltage oscillations when sudden insolation changes occur. In other words, the speed of the dc-bus voltage control loop must be adequately designed to be slower than the current control loops to guarantee no interference with each other, which could affect the quality of the current waveform injected into the grid.

Therefore, the FFCL acts through the CRG. In other words, the FFCL previously estimates the energy available in the PV

array and, hence, helps when computing the inverter active currents that will be injected into the grid. Thus, this control action contributes to reducing the settling time and overshoot that occur in the dc-bus voltage, as well as in the inverter currents during transients.

The active power generated by the PV array ($P_{\rm pv}$) is calculated as follows:

$$P_{\rm pv} = v_{\rm pv} i_{\rm pv} = (v_{\rm dc_1} + v_{\rm dc_2}) i_{\rm pv} \tag{6}$$

where $v_{\rm pv}$ and $i_{\rm pv}$ represent the PV array voltage and current, respectively, and $v_{\rm dc_1}$ and $v_{\rm dc_2}$ are the dc-bus voltages.

Assuming that the PV system handles only active energy and the grid-tied inverter currents are balanced, the active power ($P_{\rm ac}$) injected into the grid is given by

$$P_{\rm ac} = 3V_{s_{\rm rms}} I_{s_{\rm rms}} = \frac{3V_{s_p} I_{s_p}}{2} \tag{7}$$

where $V_{s_{\rm rms}}$ and $I_{s_{\rm rms}}$ represent the rms values of the fundamental utility voltage and current, respectively, and V_{s_p} and I_{s_p} are their respective peak amplitudes.

It is supposed that the PV system operates in ideal conditions, such that the system losses can be disregarded. In this case, the total active power extracted from the PV array is provided to the grid, such that $P_{\rm ac} = P_{\rm pv}$.Therefore, from (6) and (7), the utility peak current (I_{s_p}) can be estimated by

$$I_{s_p} = \frac{2 v_{\rm pv} i_{\rm pv}}{3V_{s_{p1}}} \tag{8}$$

where $v_{\rm pv}$ and $i_{\rm pv}$ are measured, while $V_{s_{p1}}$ is estimated by a PLL system and represents the peak amplitude of the utility voltage positive-sequence component.

As can be seen in Fig. 2, the $i_{\rm ff}$ is represented in the synchronous rotating frame. Thus, when I_{s_p} is transformed from the *abc*-axes into the *dq*-axes, $i_{\rm ff}$ can be computed by

$$i_{\rm ff} = \sqrt{3/2} I_{s_p}. \tag{9}$$

Therefore, $i_{\rm ff}$ is used in (3) to calculate the currents $i_{c\alpha}$ and $i_{c\beta}$. By means of (3), the inverter reference currents ($i^*_{ca}, i^*_{cb}, i^*_{cc}$) are computed by (4). Thus, as can be noted, $i_{\rm ff}$ acts to accelerate the calculation of the inverter reference currents. As a result, $i_{\rm ff}$ contributes to improve the dynamic responses of both the dc-bus voltage and grid-tied inverter currents.

As can be noted, to implement the FFCL, no additional voltage or current transducers are needed, since the quantities that compose $i_{\rm ff}$ have been previously measured or estimated.

A. PLL Scheme

Fig. 4 presents the there-phase PLL scheme implemented in this paper. The PLL system called AF-PSD-3pPLL is composed of three nonautonomous adaptive filters (AFs) and a positive-sequence detector (PSD) operating in conjunction with the 3pPLL [21]. Besides high rejection against voltage harmonics and voltage unbalances, the AF-PSD-3pPLL presents fast phase-locking.

The PLL PI controller gains ($k_{P\rm pll}$, $k_{I\rm pll}$), as well as the AF gain (K_c) shown in Fig. 4, are designed taking into account the well-known frequency response analysis [23], together with

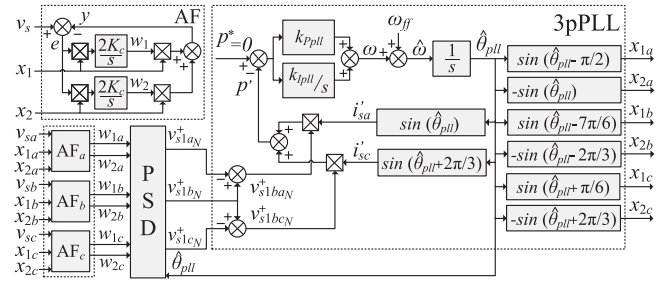

Fig. 4. Block diagram of the AF-PSD-3pPLL system.

the stability analysis presented in [21]. The gains $k_{P\rm pll}$ and $k_{I\rm pll}$ and $K_c = \mu/T_a$ are presented in Table I, where T_a is the digital signal processor (DSP) sampling time and μ is the adaptation step size of the AFs. The gain $A = \sqrt{z_1^2 + z_2^2}$ is the positive-sequence peak amplitude of the three-phase utility voltage ($A = V_{s_{p1}}$), such that $z_1 = (w_{1a} + w_{1b} + w_{1c})/3$ and $z_2 = (w_{2a} + w_{2b} + w_{2c})/3$, where $w_{1a,b,c}$ and $w_{2a,b,c}$ are the AF weights in the *abc* stationary reference frame.

IV. Controller Design of the NPC Inverter

This section presents the mathematical development for obtaining the controller design of the 3L-NPC inverter, where both the TFs of the current and voltage control loops are presented.

A. Current Control Loop

The current controllers of the 3L-NPC inverter are implemented in the three-phase stationary reference frame (*abc*-axes). The mathematical development is accomplished considering that the filtering inductances and their respective resistances are identical, such that $L_{fa} = L_{fb} = L_{fc}$ and $R_{Lfa} = R_{Lfb} = R_{Lfc}$. Thus, by means of circuit analysis performed in the inverter scheme shown in Fig. 1, the following equations can be found:

$$u_{an_\rm pwm} = v_{L_{fa}} + v_{R_{Lfa}} + v_{sa} \tag{10}$$

$$u_{bn_\rm pwm} = v_{L_{fb}} + v_{R_{Lfb}} + v_{sb} \tag{11}$$

$$u_{cn_\rm pwm} = v_{L_{fc}} + v_{R_{Lfc}} + v_{sc} \tag{12}$$

where $u_{an_\rm pwm}$, $u_{bn_\rm pwm}$, and $u_{cn_\rm pwm}$ are the respective PWM output voltages at the parallel NPC inverter terminals; $v_{L_{fa}}$, $v_{L_{fb}}$, and $v_{L_{fc}}$ are the filter inductance voltages; $v_{R_{Lfa}}$, $v_{R_{Lfb}}$, and $v_{R_{Lfc}}$ are the resistance voltages of the filter inductors; and v_{sa}, v_{sb}, and v_{sc} are the utility voltages.

Thereby, after some mathematical manipulations in (10)–(12), the open-loop TF of the physical system (G_{ps}) is given by

$$G_{ps_{a,b,c}}(s) = \frac{v_{\rm dc}}{2} \frac{1}{L_{fa,b,c} s + R_{Lfa,b,c}}. \tag{13}$$

On the other hand, based on the current control loop presented in Fig. 3, the closed-loop TF considering the PI controllers is

TABLE I
PARAMETERS ADOPTED IN THE EXPERIMENTAL TESTS

Apparent power of the unbalanced three-phase nonlinear loads			$S_a = 860$ VA, $S_b = 750$ VA, $S_c = 470$ VA
Nominal utility voltages (rms)			$V_s = 127.27$ V
Inverter inductive filters			$L_{fs} = 1.7$ mH
Resistance of the inverter inductive filters			$R_{Lfs} = 0.2\ \Omega$
Equivalent dc-bus capacitance			$C_{\mathrm{dc}} = 2350\ \mu F$
MPP dc-bus voltage			$V_{\mathrm{dc}} = 616$ V
Switching frequency of the NPC inverter			$f_{\mathrm{sw}} = 20$ kHz
Sampling frequency of the DSP A/D converter			$f_a = 60$ kHz
P&O-based MPPT step-size voltage			$\Delta v = 1$ V
P&O-based MPPT sampling time			$Ts_{\mathrm{MPPT}} = 166.67$ ms
PWM gain			$K_{\mathrm{PWM}} = 2 \times 10^{-3}$
Unbalanced nonlinear loads			
Loads	Phase A	Phase B	Phase C
Single-phase	$R = 12.5\ \Omega$	$R = 19.5\ \Omega$	$R = 58\ \Omega$
Full bridge rectifiers	$L = 15.6$ mH	$L = 24.2$ mH	$C = 940\ \mu$F
followed by RL and RC load	$L_{La} = 1.3$ mH	$L_{Lb} = 3$ mH	$L_{Lc} = 6.1$ mH

represented by

$$\frac{i_{ca,b,c}(s)}{i^*_{ca,b,c}(s)} = \frac{X_1(k_{Pi}s + k_{Ii})}{L_{fa,b,c}s^2 + (R_{Lfa,b,c} + X_1 k_{Pi})s + X_1 k_{Ii}} \tag{14}$$

where $X_1 = K_{\mathrm{PWM}} v_{\mathrm{dc}}/2$, k_{Pi} and k_{Ii} are the proportional and integral gains of the PI current controllers, and $i^*_{ca,b,c}(s)$ are the current references in the *abc*-axes.

B. DC-Bus Voltage Control Loops

The TFs of the dc-bus voltage control loop take into account the theoretical development presented in [24]. As a result, the open-loop TF of the dc-bus voltage ($G_{v_{\mathrm{dc}}}$) can be represented by

$$G_{v_{\mathrm{dc}}}(s) = \frac{vd}{v_{\mathrm{dc}} C_{\mathrm{dc}} s} \tag{15}$$

where vd represents the utility voltage into the synchronous rotating frame (d-axis), v_{dc} is the dc-bus voltage, and C_{dc} is the dc-bus equivalent capacitance.

Considering the dc-bus voltage PI controller ($\mathrm{PI}_{v_{\mathrm{dc}}}$), the closed-loop TF can be represented by

$$\frac{v_{\mathrm{dc}}(s)}{v^*_{\mathrm{dc}}(s)} = \frac{k_{Pv_{\mathrm{dc}}} vds + k_{Iv_{\mathrm{dc}}} vd}{v_{\mathrm{dc}} C_{\mathrm{dc}} s^2 + k_{Pv_{\mathrm{dc}}} vds + k_{Iv_{\mathrm{dc}}} vd} \tag{16}$$

where $k_{Pv_{\mathrm{dc}}}$ and $k_{Iv_{\mathrm{dc}}}$ are the PI controller gains (see Fig. 3).

In addition, the inherent voltage unbalances of the split capacitors placed in the inverter dc bus must be compensated. In other words, a specific dc-bus controller must be used to overcome this problem, as shown in Fig. 3. The currents that flow through the capacitors C_{dc_1} and $C_{\mathrm{dc}2}$ are considered to obtain the mathematical model of this plant, as

$$i_{C_{\mathrm{dc}_{1,2}}} = C_{\mathrm{dc}_{1,2}} \frac{dv_{\mathrm{dc}_{1,2}}}{dt}. \tag{17}$$

Applying the Laplace transform and considering $C_{\mathrm{dc}_1} = C_{\mathrm{dc}_2}$, the open-loop TF of the unbalanced dc-bus voltage controller loop ($G_{v_{\mathrm{dc}_u}}$) is given by

$$G_{v_{\mathrm{dc}_u}}(s) = \frac{v_{\mathrm{dc}_1}(s) - v_{\mathrm{dc}_2}(s)}{i_c(s)} = \frac{3}{2C_{\mathrm{dc}_1} s}. \tag{18}$$

Thus, considering the unbalanced voltage PI controller ($\mathrm{PI}_{v_{\mathrm{dc}_u}}$), the closed-loop TF is represented by

$$\frac{v_{\mathrm{dc}_1}(s) - v_{\mathrm{dc}_2}(s)}{v^*_{\mathrm{dc}_1}(s) - v^*_{\mathrm{dc}_2}(s)} = \frac{3k_{Pv_{\mathrm{dc}_u}} s + 3k_{Iv_{\mathrm{dc}_u}}}{2C_{\mathrm{dc}_1} s^2 + 3k_{Pv_{\mathrm{dc}_u}} s + 3k_{Iv_{\mathrm{dc}_u}}} \tag{19}$$

where $k_{Pv_{\mathrm{dc}_u}}$ and $k_{Iv_{\mathrm{dc}_u}}$ are the PI controller gains (see Fig. 3).

Once the open-loop TFs (G_{ps}, $G_{v_{\mathrm{dc}}}$, and $G_{v_{\mathrm{dc_u}}}$) are obtained, the current and voltage PI controllers can be tuned. The procedure used for tuning all the controllers was based on the frequency response method, via Bode diagram, presented in [23]. In this method, the design specifications are the phase-margin (PM) and the crossover frequency at 0-dB gain. Thus, the PI controllers will provide the angular contributions to meet the specified PMs and the proper gains to ensure that the compensated systems present the specified crossover frequencies at 0 dB.

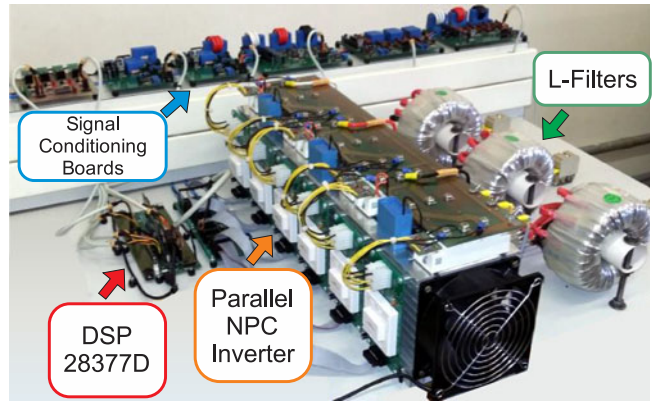

Fig. 5. Prototype setup.

V. EXPERIMENTAL RESULTS

The experimental setup of the PV system was constructed based on the scheme shown in Fig. 1 and is shown in Fig. 5. The digital implementation was performed by using the DSP (TMDXCNCD28377D—*Texas Instruments*), in which the current and dc-bus voltage controllers were embedded, as well as the FFCL, P&O-based MPPT, CRG, and PLL algorithms. The 3L-NPC inverter was implemented using six insulated-gate bipolar transistor modules (SKM100GB 12T4—*Semikron*), with their proper drivers, and six fast recovery diodes (DSEI 60 06A—*IXYS*). The LEM LA 100-Pand LEM LV 25P transducers were used to measure the PV system currents and voltages, respectively, whereas the PV array string is composed of 20 series-connected PV panels (SW 245—*SolarWorld*).

The main parameters employed in the experimental tests are presented in Table I, while Table II presents the design specifications of the PI controllers (PMs and the crossover frequencies), and all the PI controller gains.

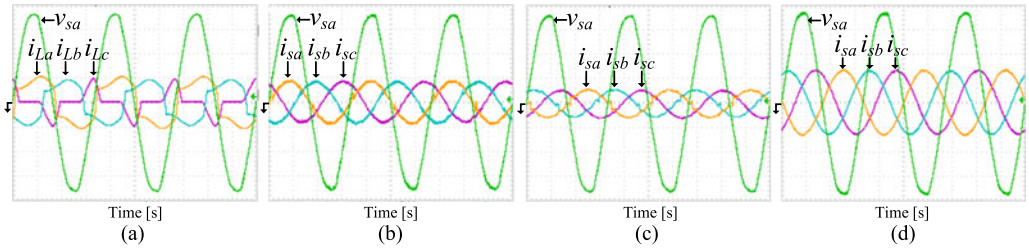

Fig. 6. Utility voltage (v_{sa}), load currents (i_{La}, i_{Lb}, i_{Lc}), and compensated source currents (i_{sa}, i_{sb}, i_{sc}) of the PV system (50 V/div, 10 A/div, 5 ms/div). (a) Utility voltage and load currents. (b) OPM 1: only active power-line conditioning ($P_{\rm pv} = 0$ W). (c) OPM 2: active power injection plus active power-line conditioning ($P_{\rm pv} \cong 3600$ W). (d) OPM 3: total active power injection into the grid ($P_{\rm pv} \cong 3600$ W and $P_L = 0$ W).

TABLE II
DESIGN SPECIFICATIONS AND GAINS OF THE PI CONTROLLERS

PI-MR current controllers	
PI_i crossover frequency	$\omega_{ci} = 1.2566e^4$ rad/s
PI_i phase margin	$\mathrm{PM}_i = 85^\circ$
PI_i current controller gains	$k_{Pi} = 351.29$ $k_{Ii} = 4.2717e^5$
Crossover frequencies of the Current MR controller	$\omega_{c1} = \omega_{c3} = \omega_{c5} = \omega_{c7} = \omega_{c9} = 1.2566e^4 \mathrm{rad}/s$
Current MR controller gains	$k_1 = 12555$; $k_3 = 12465$; $k_5 = 12284$; $k_7 = 12012$; $k_9 = 11650$
dc-bus voltage controllers	
$\mathrm{PI}_{v_{\rm dc}}$ crossover frequency	$\omega_{v_{\rm dc}} = 28.274$ rad/s
$\mathrm{PI}_{v_{\rm dc}}$ phase margin	$\mathrm{PM}_{v_{\rm dc}} = 75^\circ$
$\mathrm{PI}_{v_{\rm dc}}$ voltage controller gains	$k_{Pv_{\rm dc}} = 0.1797$ $k_{Iv_{\rm dc}} = 1.3615$
$\mathrm{PI}_{v_{{\rm dc}u}}$ crossover frequency	$\omega_{v_{{\rm dc}u}} = 14.5932$ rad/s
$\mathrm{PI}_{v_{{\rm dc}u}}$ phase margin	$\mathrm{PM}_{v_{{\rm dc}u}} = 82^\circ$
$\mathrm{PI}_{v_{{\rm dc}u}}$ unbalance controller gains	$k_{Pv_{{\rm dc}u}} = 0.0453$ $k_{Iv_{{\rm dc}u}} = 0.0929$
PLL parameters and controller gains	
$\mathrm{PI}_{\rm pll}$ controller gains	$k_{P\rm pll} = 141.7$; $k_{I\rm pll} = 7777.4$
AF gain	$K_c = 300$
AF adaptation step size	$\mu = 0.005$

TABLE III
THDS AND RMS VALUES OF THE LOAD AND SOURCE CURRENTS AND PFS

Operation Modes	Total harmonic distortions (THD %)					
	i_{sa}	i_{sb}	i_{sc}	i_{La}	i_{Lb}	i_{Lc}
OPM 1	4.1	2.6	2.6	26.5	23.3	56.1
OPM 2	8.2	6.6	3.8	26.5	23.3	56.1
OPM 3	1.7	1.5	1.5	—	—	—
	rms Currents (A)					
OPM 1	5.23	5.11	4.95	6.91	5.99	3.72
OPM 2	3.47	3.17	3.30	6.91	5.99	3.72
OPM 3	8.07	8.01	8.04	—	—	—
	Power Factor					
OPM 1	1.0	1.0	1.0	0.93	0.92	0.78
OPM 2	0.99	0.99	0.99	0.93	0.92	0.78
OPM 3	1.0	1.0	1.0	—	—	—

Fig. 6 shows the static behavior of the PV system taking into account three different operation modes (OPMs), which are described as follows: OPM 1 performs only active power-line conditioning; OPM 2: performs active power injection plus active power-line conditioning; and OPM 3: performs only active power injection. In Fig. 6, the following quantities are shown: phase "a" utility voltage (v_{sa}), compensated source currents (i_{sa}, i_{sb}, i_{sc}), and load currents (i_{La}, i_{Lb}, i_{Lc}).

Fig. 6(a) shows the load currents related to the nonlinear and unbalanced loads presented in Table I, in conjunction with the phase "a" utility voltage (v_{sa}). Fig. 6(b) presents the experimental results for the OPM 1, where $P_{\rm pv}$ is zero and the nonlinear loads are connected to the grid. In this case, the PV system performs only the active power-line conditioning. As can be seen, the compensated source currents are always sinusoidal and in phase with the utility voltage. In OPM 2, $P_{\rm pv}$ is higher than the load active power P_L. In this case, $P_{\rm pv}$ is consumed by the load and the remaining power is injected into the grid, as shown in Fig. 6(c). OPM 3 is shown in Fig. 6(d), where the total active power produced by the PV array is injected into the grid ($P_{\rm pv}$ is around 3600 W). As can be seen in Fig. 6(c) and (d), the source currents are sinusoidal and in opposite phase with the respective utility voltages.

Table III presents the total harmonic distortion (THD) of the compensated source currents and load currents. As can be noted, in all OPMs, the THDs of the compensated source currents were significantly reduced. Table III also shows the rms currents and PFs with and without active power-line compensation. As can be observed, an effective PF correction was carried out.

Fig. 7 presents the dynamic response of the dc-bus voltages ($v_{\rm dc}$, $v_{\rm dc_1}$, $v_{\rm dc_2}$) and the source current (i_{sa}), when the PV array is abruptly connected and disconnected from the inverter dc bus, which represents a sudden solar radiation change.

In Fig. 7(a) and (c), the PV array remains disconnected from the dc bus for up to 50 ms. After that, the PV array is connected again. As can be seen, the dynamic response of the PV system without the FFCL [see Fig. 7(a)] is lower than observed when the PV system is operating with the FFCL [see Fig. 7(c)]. The same dynamic behavior can be observed in Fig. 7(b) and (d), where the PV array remains connected for up to 50 ms, and after that it is disconnected again. Fig. 7(b) shows the PV system dynamic response without the FFCL, while in Fig. 7(d), the PV system is operating with the FFCL. Furthermore, Fig. 7(c) and (d) show that use of the FFCL contributes to increasing the speed of the transient responses of the compensated source current (i_{sa}), as well as assuring that there is no oscillation in the dc-bus voltages during the PV array transients. Fig. 7 also shows that there is no voltage unbalance in the dc-bus capacitors, meaning that the dc-bus voltage unbalance controller is operating properly.

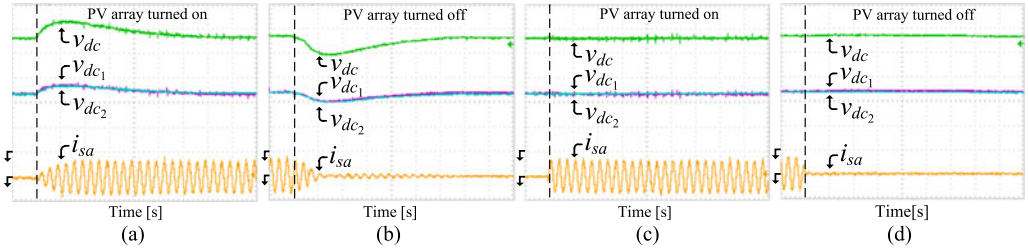

Fig. 7. DC-bus voltages ($v_{\rm dc}$, $v_{\rm dc_1}$, $v_{\rm dc_2}$) and source current (i_{sa}) considering OPM 3 (100 V/div, 20 A/div, 50 ms/div). (a) PV array connection without FFCL. (b) PV array disconnection without FFCL. (c) PV array connection with FFCL. (d) PV array disconnection with FFCL.

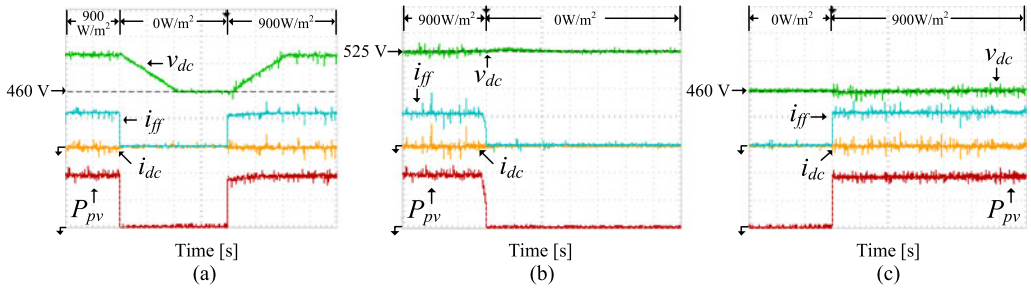

Fig. 8. DC-bus voltage ($v_{\rm dc}$), FFC ($i_{\rm ff}$), dc-bus controller current ($i_{\rm dc}$), and PV array power ($P_{\rm pv}$) for abrupt solar radiation change considering OPM 3 with FFCL (50 V/div, 14 A/div, 2 kW/div). (a) Solar radiation transient (5 s/div). (b) Solar radiation step down (100 ms/div). (c) Solar radiation step up (100 ms/div).

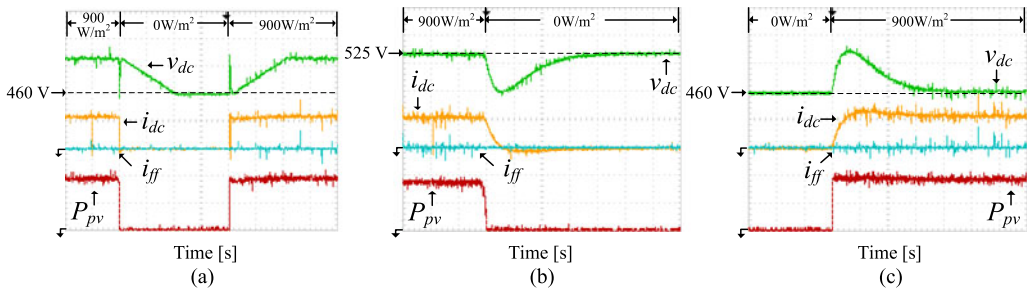

Fig. 9. DC-bus voltage ($v_{\rm dc}$), FFC ($i_{\rm ff}$), dc-bus controller current ($i_{\rm dc}$), and PV array power ($P_{\rm pv}$) for abrupt solar radiation change considering OPM 3 without FFCL (50 V/div, 14 A/div, 2 kW/div). (a) Solar radiation transient (5 s/div). (b) Solar radiation step down (100 ms/div). (c) Solar radiation step up (100 ms/div).

Fig. 8 shows the FFC acting to improve the dynamic response of the PV system. Up to 10 s, the PV system is operating normally. At this moment, the PV array is disconnected and reconnected again after 20 s. Details related to the transients can be observed in Fig. 8(b) and (c), where no oscillation is observed in the dc-bus voltage. During this time interval, in which the PV array is disconnected, the PV system operates in OPM 1 and the dc-bus voltage reference is set to $v_{\rm dc}^* =$ 460 V. When the PV array is reconnected, the MPP is reached in around 8 s, such that $v_{\rm dc}^* = 525$ V. Now, $v_{\rm dc}^*$ is defined again by the MPPT algorithm.

Fig. 9 shows the results obtained when the FFCL is not considered. As can be observed, the dynamic response of the PV system is slower. This happens because the dc-bus voltage control loop must necessarily be designed to be slower than the current control loops, as previously discussed in Section II.

Fig. 10 presents the results when step loads are performed (100% to 0% and 0 to 100%). It can be noted that even when the FFCL is acting, the PV system dynamic response is not improved. This happens due to the FFCL acts only on the atmospheric disturbances to which the PV array is subjected.

VI. Conclusion

This paper presented a single-stage three-phase grid-tied PV system using the three-level NPC inverter. In order to improve the PV system dynamic response, a current FFCL acting to speed up the computation of the inverter current references was proposed. Thus, improved PV system performance was achieved when the PV array was subjected to climatic variations, such as sudden insolation changes. As a result, both the dc-bus voltage and grid-tied inverter currents dynamic behaviors were improved with respect to the setting time and overshoot/undershoot). In addition, the PV system static behavior operating with active power-line conditioning was verified, where an effective PF correction was achieved. The performance and feasibility of the PV system were evaluated by means of

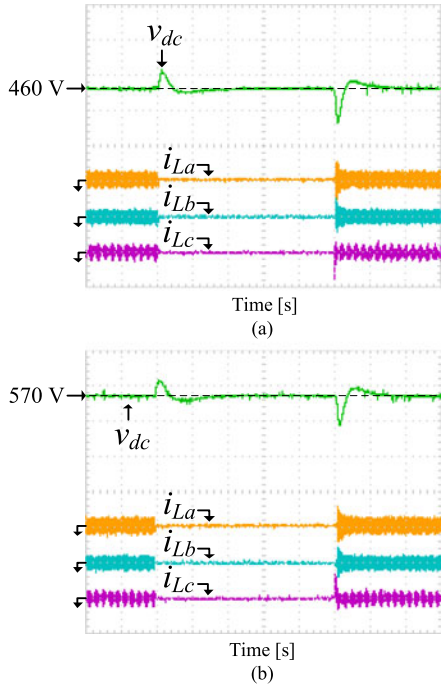

Fig. 10. DC-bus voltage ($v_{\rm dc}$) and load currents (i_{La}, i_{Lb}, i_{Lc}) for step load (100 V/div, 50 A/div, 500 ms/div). (a) OPM1/FFCL. (b) OPM2/FFCL.

extensive experimental results, validating the theoretical development.

References

[1] S. B. Kjaer, J. K. Pedersen, and F. Blaabjerg, "A review of single-phase grid-connected inverters for photovoltaic modules," *IEEE Trans. Ind. Appl.*, vol. 41, no. 5, pp. 1292–1306, Sep./Oct. 2005.

[2] Y. Kim, H. Cha, B. M. Song, and K. Y. Lee, "Design and control of a grid-connected three-phase 3-level NPC inverter for building integrated photovoltaic systems," in *Proc. IEEE PES Innovative Smart Grid Technol.*, Washington, DC, USA, 2012, pp. 1–7.

[3] F. J. Lin, K. C. Lu, T. H. Ke, B. H. Yang, and Y. R. Chang, "Reactive power control of three-phase grid-connected PV system during grid faults using Takagi–Sugeno–Kang probabilistic fuzzy neural network control," *IEEE Trans. Ind. Electron.*, vol. 62, no. 9, pp. 5516–5528, Sep. 2015.

[4] M. M. R. Singaravel and S. A. Daniel, "MPPT with single DC–DC converter and inverter for grid-connected hybrid wind-driven PMSG–PV system," *IEEE Trans. Ind. Electron.*, vol. 62, no. 8, pp. 4849–4857, Aug. 2015.

[5] A. Yazdani and P. P. Dash, "A Control methodology and characterization of dynamics for a photovoltaic (PV) system interfaced with a distribution network," *IEEE Trans. Power Del.*, vol. 24, no. 3, pp. 1538–1551, Jul. 2009.

[6] S. A. O. Silva, L. B. G. Campanhol, V. D. Bacon, and L. P. Sampaio, "Single-phase grid-connected photovoltaic system with active power line conditioning," *Brazilian Power Electron. J.*, vol. 20, no. 1, pp. 8–18, Feb. 2015.

[7] F. M. Oliveira, S. A. O. Silva, F. R. Durand, L. P. Sampaio, V. D. Bacon, and L. B. G. Campanhol, "Grid-tied photovoltaic system based on PSO MPPT technique with active power line conditioning," *IET Power Electron.*, vol. 9, no. 6, pp. 1180–1191, Apr. 2016.

[8] M. C. Cavalcanti, A. M. Farias, K. C. Oliveira, F. A. S. Neves, and J. L. Afonso, "Eliminating leakage currents in neutral point clamped inverters for photovoltaic systems," *IEEE Trans. Ind. Electron.*, vol. 59, no. 1, pp. 435–443, Oct. 2011.

[9] N. Vázquez, M. Rosas, C. Hernández, E. Vázquez, and F. J. Perez-Pinal, "A new common-mode transformerless photovoltaic inverter," *IEEE Trans. Ind. Electron.*, vol. 62, no. 10, pp. 6381–6391, Oct. 2015.

[10] W. Li, Y. Gu, H. Luo, W. Cui, X. He, and C. Xia, "Topology review and derivation methodology of single-phase transformerless photovoltaic inverters for leakage current suppression," *IEEE Trans. Ind. Electron.*, vol. 62, no. 7, pp. 4537–4551, Jul. 2015.

[11] Y. Tang, W. Yao, P. C. Loh, and F. Blaabjerg, "Highly reliable transformerless photovoltaic inverters with leakage current and pulsating power elimination," *IEEE Trans. Ind. Electron.*, vol. 63, no. 2, pp. 1016–1026, Feb. 2016.

[12] W. Libo, Z. Zhengming, and L. Jianzheng, "A single-stage three-phase grid-connected photovoltaic system with modified MPPT method and reactive power compensation," *IEEE Trans. Power Electron.*, vol. 22, no. 4, pp. 881–886, Dec. 2007.

[13] S. M. Reza Touse, M. H. Moradi, N. S. Basir, and M. Nemati, "A function-based maximum power point tracking method for photovoltaic systems," *IEEE Trans. Power Electron.*, vol. 31, no. 3, pp. 2120–2128, Mar. 2016.

[14] K. Ishaque, Z. Salam, M. Amiad, and S. Mekhilef, "An improved particle swarm optimization (PSO)-based MPPT for PV with reduced steady-state oscillation," *IEEE Trans. Power Electron.*, vol. 27, no. 8, pp. 3627–3638, Aug. 2012.

[15] M. A. G. Brito, L. Galotto, L. P. Sampaio, G. A. Melo, and C. A. Canesin, "Evaluation of the main MPPT techniques for photovoltaic applications," *IEEE Trans. Ind. Electron.*, vol. 60, no. 3, pp. 1156–1167, Mar. 2013.

[16] C. Roncero-Clemente, O. Husev, E. Romero-Cadaval, J. Martins, D. Vinnikov, and M. I. Milanes-Montero, "Three-phase three-level neutral-point-clamped qZ source inverter with active filtering capabilities," in *Proc. 9th Int. Conf. Compat. Power Electron.*, Costa da Caparica, Portugal, 2015, pp. 216–220.

[17] T. Geury, S. Pinto, and J. Gyselinck, "Three-phase power controlled PV current source inverter with incorporated active power filtering," in *Proc. 39th IEEE Ind. Electron. Conf.*, Vienna, Austria, 2013, pp. 1374–1379.

[18] C. H. Chang, Y. H. Lin, Y. M. Chen, and Y. R. Chang, "Simplified reactive power control for single-phase grid-connected photovoltaic inverters," *IEEE Trans. Ind. Electron.*, vol. 61, no. 5, pp. 2286–2296, May 2014.

[19] *IEEE Standard Definitions for the Measurement of Electric Power Quantities Under Sinusoidal, Nonsinusoidal, Balanced, or Unbalanced Conditions*, IEEE Standard 1459-2010 (Revision of IEEE Std 1459-2000), Mar. 2010, pp. 1–50.

[20] S. Sezen, A. Aktas, M. Ucar, and E. Ozdemir, "A three-phase three-level NPC inverter based grid-connected photovoltaic system with active power filtering," in *Proc. 16th Int. Power Electron. Motion Control Conf. Expo.*, Antalya, Turkey, 2014, pp. 1331–1335.

[21] V. D. Bacon and S. A. O. Silva, "Performance improvement of a three-phase phase-locked-loop algorithm under utility voltage disturbances using non-autonomous adaptive filters," *IET Power Electron.*, vol. 8, no. 11, pp. 2237–2250, Nov. 2015.

[22] S. Buso and P. Mattavelli, Digital Control in Power Electronics. Lincoln, NE, USA: Morgan & Claypool, 2006.

[23] B. A. Angélico, L. B. G. Campanhol, and S. A. O. Silva, "Proportional–integral/proportional–integral–derivative tuning procedure of a single-phase shunt active power filter using Bode diagram," *IET Power Electron.*, vol. 7, no. 10, pp. 2647–2659, Aug. 2014.

[24] L. B. G. Campanhol, S. A. O. Silva, and A. Goedtel, "Application of shunt active power filter for harmonic reduction and reactive power compensation in three-phase four-wire systems," *IET Power Electron.*, vol. 7, no. 11, pp. 2825–2836, Nov. 2014.

Leonardo Bruno Garcia Campanhol was born in Rolândia, Brazil, in 1986. He received the B.S. degree in industrial automation technology and the M.S. degree in electrical engineering from the Federal University of Technology, Cornélio Procópio, Brazil, in 2009 and 2012, respectively. He is currently working toward the Ph.D. degree at the São Carlos Engineering School, University of São Paulo, São Carlos, Brazil.

Since 2013, he has been with the Department of Electrical Engineering, Federal University of Technology, Apucarana, Brazil, where he is currently an Associate Professor of electrical engineering. His research interests include power electronics applications involving unified power quality conditioner systems, active power-line filters, photovoltaic systems, power quality, and digital signal processing and applications.

Mr. Campanhol is a member of the Brazilian Power Electronics Society.

Sérgio Augusto Oliveira da Silva (M'13) was born in Joaquim Távora, Brazil, in 1964. He received the B.S. and M.S. degrees in electrical engineering from the Federal University of Santa Catarina, Florianopolis, Brazil, in 1987 and 1989, respectively, and the Ph.D. degree from the Federal University of Minas Gerais, Belo Horizonte, Brazil, in 2001.

Since 1993, he has been with the Department of Electrical Engineering, Federal University of Technology, Cornélio Procópio, Brazil, where he is currently a full Professor of electrical engineering and Coordinator of the Power Electronics, Power Quality and Renewable Energies Laboratory. His research interests include power electronics applications involving uninterruptible power supply systems, active power-line filters, photovoltaic systems, control systems, and power quality.

Prof. da Silva is a member of the Brazilian Power Electronics Society and the IEEE Industrial Electronics Society.

Azauri Albano de Oliveira, Jr. was born in 1955. He received the B.S and M.S. degrees in electrical/electronic engineering from the São Carlos Engineering School (EESC), University of São Paulo (USP), São Carlos, Brazil, in 1977 and 1984, respectively, and the Ph.D. degree in electrical engineering from the Polytechnic School, University of São Paulo, in 1991.

Since 1978, he has been with the Department of Electrical and Computing Engineering, EESC, USP, where he is currently a Professor of electrical engineering and the Coordinator of the Power Electronics and Control Laboratory. His research interests include power electronics, electric machinery drives, wireless power transfer, and engineering education.

Vinícius Dário Bacon was born in Arapongas, Brazil, in 1991. He received the B.S. and M.S. degrees in electrical engineering in 2013 and 2015, respectively, from the Federal University of Technology (UTFPR-CP), Cornélio Procópio, Brazil, where he is currently working toward the Ph.D. degree.

Since 2016, he has been with the Department of Electrical Engineering, UTFPR-CP, where he is currently an Adjunct Professor of electrical engineering. His current research interests include power quality, active power filters, renewable energies, and digital signal processing and applications.

Mr. Bacon is a member of the Brazilian Power Electronics Society.